Storm Labeling in Three Dimensions (SL3D): A Volumetric Radar Echo and Dual-Polarization Updraft Classification Algorithm

MARIUSZ STARZEC

Department of Atmospheric Sciences, University of North Dakota, Grand Forks, North Dakota

CAMERON R. HOMEYER

School of Meteorology, University of Oklahoma, Norman, Oklahoma

GRETCHEN L. MULLENDORE

Department of Atmospheric Sciences, University of North Dakota, Grand Forks, North Dakota

(Manuscript received 4 March 2016, in final form 19 December 2016)

ABSTRACT

This study presents a new storm classification method for objectively stratifying three-dimensional radar echo into five categories: convection, convective updraft, precipitating stratiform, nonprecipitating stratiform, and ice-only anvil. The Storm Labeling in Three Dimensions (SL3D) algorithm utilizes volumetric radar data to classify radar echo based on storm height, depth, and intensity in order to provide a new method for updraft classification and improve upon the limitations of traditional storm classification algorithms. Convective updrafts are identified by searching for three known polarimetric radar signatures: weak-echo regions (bounded and unbounded) in the radar reflectivity factor at horizontal polarization (Z_{H}), differential radar reflectivity (Z_{DR}) columns, and specific differential phase (K_{DP}) columns. Additionally, leveraging the three-dimensional information allows SL3D to improve upon missed identifications of weak convection and intense stratiform rain in traditional two-dimensional classification schemes. This study presents the results of applying the SL3D algorithm to several cases of high-resolution three-dimensional composites of NEXRAD WSR-88D data in the contiguous United States. Comparisons with a traditional algorithm that uses two-dimensional maps of Z_{H} are also shown to illustrate the differences of the SL3D algorithm.

1. Introduction

Regions of convective and stratiform precipitation are known to differ considerably in terms of 1) microphysical composition and associated precipitation rates (e.g., Houghton 1968); 2) thermodynamic properties including diabatic heating rates, perturbations to the altitude of the environmental melting (or freezing) level, and related storm divergence profiles (e.g., Johnson 1984; Houze 1989; Mapes and Houze 1993); and 3) their relative frequency of occurrence across the globe (e.g., Schumacher and Houze 2003). Recognition of these differences has motivated several previous studies to develop methods that objectively identify convective and stratiform precipitation in radar and satellite observations in order to enable improvements in our understanding of their differences and associated physical and dynamical processes (e.g., Adler and Negri 1988; Williams and Ecklund 1995; Steiner et al. 1995; DeMott et al. 1995; Anagnostou and Kummerow 1997; Hong et al. 1999; Anagnostou 2004; Bringi et al. 2009; Yang et al. 2013).

One of the most well-known and utilized schemes for convective-stratiform classification using ground-based radar observations is the Steiner et al. (1995) method, hereafter referred to as SHY. SHY employs a three-step procedure to distinguish between convective and stratiform precipitation using observations at the lowest elevation in a radar volume. First, any value of the radar reflectivity factor at horizontal polarization (Z_{H}) that exceeds a specified threshold is considered convective. Second, an additional exceedance threshold is used to identify previously unclassified convective elements if the Z_{H} at a grid point surpasses the mean background

---

Corresponding author e-mail: Mariusz Starzec, mariusz.starzec@my.und.edu

DOI: 10.1175/MWR-D-16-0089.1

© 2017 American Meteorological Society. For information regarding reuse of this content and general copyright information, consult the AMS Copyright Policy (www.ametsoc.org/PUBSReuseLicenses).

Z_H over a set radius [similar to that of Adler and Negri (1988)]. Third, a convective radius of influence is applied to all identified locations of convection from steps 1 and 2 to broaden the horizontal extent of the convective classification to regions of similarly intense precipitation. In other words, depending on the magnitude of Z_H relative to the mean background value, all points within a certain radius are labeled as convective.

Many studies have built upon the SHY procedure by incorporating vertical information in the classification to improve its performance, particularly in cases where convection is weak, stratiform precipitation is intense, or convective regions are strongly tilted in the vertical (thereby inadvertently decoupling convective precipitation at low altitudes from its source aloft). Biggerstaff and Listemaa (2000) added a step to compute the vertical lapse rate of Z_H in the 3-km layer above the Z_H column-maximum value to improve the skill of the convective classification in the SHY method, and a "brightband" (Z_H maximum occurring near the melting level in stratiform precipitation) detection method to improve the stratiform classification. More recently, Powell et al. (2016) incorporated a range-dependent SHY-based classification to low elevations of single-radar observations in their native polar coordinates to better identify shallow convection and improve precipitation estimation. Feng et al. (2011) focused on the top-of-the-atmosphere radiation budget of convective systems and added a convectively generated anvil [i.e., an anvil resulting from direct detrainment from the convective updraft; e.g., Mullendore et al. (2009)] cloud classification to the SHY scheme. Feng et al. (2011) used five constant-altitude levels from three-dimensional composites of multiple ground-based radars to distinguish between convective, stratiform, and anvil clouds.

While the aforementioned studies incorporated vertical storm information in the SHY procedure, the primary classification between convective and stratiform precipitation in SHY-based algorithms and similar approaches is completed using a single low-altitude map of Z_H. For research purposes such as quantitative precipitation estimation, SHY-based methods applied to single-radar observations can be adequate. However, the reliance of SHY-based methods on low-altitude observations alone (typically at a level of 2–3 km) limits their utility for other research topics that require knowledge on the vertical structure of convection. For example, information on the extent and depth of convection is a necessary element of analysis for studies on convective mass transport, cloud microphysics, diabatic heating, and gravity wave generation (e.g., Kuo and Anthes 1984; Nuret and Chong 1998; Alexander 2004; Schumacher et al. 2004; Mullendore et al. 2005; Barth et al. 2007; Park et al. 2009; Homeyer et al. 2014; Srinivasan et al. 2014). In addition, the use of stringent low-altitude Z_H thresholds may misclassify weak and/or shallow convection as stratiform rain or intense stratiform rain as convection, subsequently introducing biases in the analysis of precipitating systems. Methods that leverage the three-dimensional information widely available in ground- and satellite-based radar observations are required to overcome these limitations.

In this study, we introduce a method for classifying radar echo using three-dimensional high-resolution composites of radar observations from the Next Generation Weather Radar (NEXRAD) Weather Surveillance Radar-1988 Doppler (WSR-88D) network (Crum and Alberty 1993). We call this method the Storm Labeling in Three Dimensions (SL3D) algorithm. The SL3D algorithm uses the vertical depth and echo-top altitude of Z_H, additional dual-polarization (or polarimetric) radar quantities, and the altitude of the environmental melting level to stratify radar echo into five categories (described in section 3 below). We use several cases of varying organization, complexity, and regionality to demonstrate the performance of the SL3D algorithm and compare it to the traditional SHY approach. The primary goal of SL3D is to enable new analyses on topics that require information on vertical storm structure by producing a regionally unspecific classification of precipitating systems using three-dimensional radar observations.

2. Radar data

The radar data used in this study are three-dimensional composites of NEXRAD WSR-88D observations, where the volume data from individual radars are provided by the National Centers for Environmental Information (NCEI; National Weather Service 1991). Radar composites are created following the methods outlined in Homeyer (2014) and updated in Homeyer and Kumjian (2015). In short, observations from each radar are binned in space and time at 5-min intervals in a volume with 0.02° (~2 km) latitude–longitude grid spacing and 1-km grid spacing in the vertical. For binning, observations are weighted out to 300 km in range and within 5 min of the composite time using a Gaussian function. Grid volumes with large cumulative bin weights (i.e., the sum weight of all observations contributing to a grid volume) and a high fraction of echo detection in contributing radar scans are retained for analysis. The largest weights are given to observations closest to a radar location and closest in time to that of the composite. The time-binning component is the only difference from the procedure outlined in Homeyer and Kumjian (2015); hence, no interpolation is performed on the individual radar scans in time or space. Each composite contains up to four polarimetric variables for analysis: Z_H, the differential radar reflectivity

Z_{DR}, the specific differential phase K_{DP}, and a copolar correlation coefficient ρ_{HV}. Composites during the years 2013–present contain all four variables since the upgrade of the NEXRAD WSR-88D network to dual-polarization was completed in early 2013, while composites for cases prior to 2013 contain only Z_{H}.

The polarimetric variables from NEXRAD radars provide information on the size, shape and/or orientation, concentration, and phase of precipitable hydrometeors. For example, Z_{H} and Z_{DR} convey information about the size and shape of the largest hydrometeors in a sample volume, respectively, while K_{DP} is indicative of the presence of nonspherical hydrometeors in the beam volume. If particles are small compared to the wavelength of the radar, positive values of Z_{DR} and K_{DP} indicate scatterers with horizontal-to-vertical axis ratios greater than 1, such as raindrops, while negative values represent scatterers with horizontal-to-vertical axis ratios of less than 1. Alternatively, ρ_{HV} enables discrimination between meteorological and nonmeteorological echoes and detection of volumes with mixed-phase (water and ice) precipitation. Meteorological scatterers have ρ_{HV} near 1 for volumes with uniform particle phases. In mixed-phase regions, ρ_{HV} reduces to values as low as 0.8 and can be even lower in the presence of large hail. Nonmeteorological scatterers typically have ρ_{HV} values below 0.5. While ρ_{HV} is not used in the SL3D classification, echo with ρ_{HV} values below the 0.5 threshold are removed from the polarimetric radar composites prior to analysis in this study. More information on the physical meaning of each polarimetric radar variable is available in textbooks (e.g., Doviak and Zrnić 1993; Bringi and Chandrasekar 2001) and review papers (e.g., Herzegh and Jameson 1992; Zrnić and Ryzhkov 1999; Straka et al. 2000; Ryzhkov et al. 2005b; Kumjian 2013a,b,c).

The Z_{H} field may contain considerable bias as a result of beam broadening, partial or complete beam shielding, attenuation by atmosphere and hydrometeors, and sidelobe contamination. The Z_{H} observations may also contain artifacts such as ground clutter, second-trip echoes, and three-body scatter spikes. The dual-polarization variables (Z_{DR}, K_{DP}, and ρ_{HV}) are subject to substantial biases and artifacts, some of which are unique compared to traditional single-polarization variables such as Z_{H}. Often, ρ_{HV} is the least impacted by biases and/or artifacts, with many nontypical values in precipitation being microphysically informative. For example, a reduction in ρ_{HV} near the melting level in stratiform rain regions is present because of the coexistence of liquid and frozen hydrometeors in the radar volume. We find that K_{DP} suffers from a large amount of random noise but is not affected by calibration errors and systematic biases. Meanwhile, Z_{DR} is largely sensitive to calibration errors and is often systematically biased up to ±0.5 dB in observations from WSR-88Ds (e.g., Cunningham et al. 2013; Homeyer and Kumjian 2015). As a result, we correct for systematic Z_{DR} biases in individual radar scans prior to their inclusion in the composites using a ‘‘natural scatterer’’ approach (e.g., Ryzhkov et al. 2005a). We do not correct for well-known artifacts such as nonuniform beam filling, differential attenuation, or depolarization of the radar beam, as these are both difficult to detect objectively and are often insignificant relative to the scale of the radar composites [see Homeyer and Kumjian (2015) for additional detail and justification].

3. SL3D algorithm

The storm classification algorithm used in this study (SL3D) stratifies radar echo into five categories: convection, convective updraft, precipitating stratiform, nonprecipitating stratiform, and ice-only anvil. In summary, the objective of the SL3D convective classification is to identify precipitation that is directly generated by convective motions (i.e., strong vertical motion or ‘‘updrafts’’). Precipitating (nonprecipitating) stratiform encompasses any mixed-phase cloud that does not contain convective updrafts and is (is not) precipitating. Anvil is considered to be ice-only cloud resulting from upper-tropospheric detrainment of ice crystals by convection or advected from a convectively generated stratiform region. More detailed descriptions of the classification categories are defined in their corresponding sections below and a summary of the criteria applied to the radar observations is presented in Table 1. It is important to note that the convection classification occurs first and is incrementally followed by the stratiform (precipitating and nonprecipitating) and anvil classifications. Convective echo cannot be relabeled as stratiform or anvil. Similarly, echo identified as stratiform cannot be relabeled as anvil. Once the precipitating and nonprecipitating echo regions are identified, echo may be identified as convective updraft within 12 km of any echo classified as convection if one of several conditions are met; these conditions are outlined below.

SL3D incorporates information from the atmospheric environment. Namely, the altitude of the 0°C level (i.e., the melting level) is used, which we obtain from radiosonde observations for the cases presented in this study. While it is possible to couple melting-layer identification algorithms to SL3D using the radar observations alone (e.g., Giangrande et al. 2008), it is outside the scope of this study to evaluate and determine the sensitivity to each method. Since any objective classification is prone to error, it is the authors’ preference to limit such error

TABLE 1. The criteria used for classification into the five SL3D categories, where Z_H is horizontally polarized reflectivity, Z_{Hmax} is the column-maximum Z_H, and Z_{Melt} is the height of the melting layer.

Classification	Criteria
Convection	$Z_H = 25$ dBZ echo-top altitude ≥ 10 km, or Z_H peakedness exceeding threshold in at least 50% of the echo column between the surface and 9 km, or $Z_H \geq 45$ dBZ above Z_{Melt}
Precipitating stratiform	$Z_H \geq 20$ dBZ at 3 km or $Z_H \geq 10$ dBZ below 3 km
Nonprecipitating stratiform	No echo or $Z_H < 20$ dBZ at 3 km, and echo present below 5 km
Anvil	No echo at or below 5-km altitude, but echo present above Z_{Melt}
Updraft	$Z_{Hmax} \geq 40$ dBZ and $\partial Z_H/\partial z \geq 8$ dBZ km^{-1} with echo in at least six of eight horizontally adjacent grid volumes, or $Z_H \geq 15$ dBZ and $Z_{DR} \geq 1.5$ dBZ extending at least 1 km above Z_{Melt}, or $Z_H \geq 30$ dBZ and $K_{DP} \geq 0.5°$ km^{-1} extending at least 1 km above Z_{Melt}

sources for the SL3D algorithm and specify the altitude of the melting level.

a. *Convection and stratiform*

As outlined in the introduction, there are distinct microphysical and thermodynamic differences between convective and stratiform precipitation. Convective precipitation occurs when strong, deep mesoscale uplift and/or positive buoyancy leads to the development and growth of cloud particles. As the droplets are lofted into the middle troposphere, they freeze and grow rapidly by the collection and glaciation of additional supercooled liquid water (e.g., Churchill and Houze 1984). These updrafts can loft precipitable particles into the upper troposphere and thereby result in deep, vertically erect columns of high-Z_H values observed by radar. Updrafts can eject large amounts of ice crystals in the upper troposphere, while large, precipitation-sized particles fall out of the updraft and reach the surface as precipitation. As the particles descend, they melt, collide, and coalesce with other particles, which lead to even higher Z_H near the surface.

Stratiform precipitation results from weak mesoscale ascent at altitudes typically above the freezing level that leads to the formation, growth, and fallout of ice crystals to lower altitudes. Upper-level detrainment from deep convection is often a common source of ice crystals in stratiform regions. Ice crystals can also be actively generated in the stratiform region above the melting level (e.g., Braun and Houze 1994). The falling ice crystals in a stratiform system aggregate, which leads to moderate rates of precipitation (relative to that in convection). If the aggregates descend below the melting level, they are often visible in radar observations as a shallow layer of elevated Z_H (i.e., the bright band) or reduced ρ_{HV} immediately below the melting-level altitude.

While the vertical structures of convective and stratiform systems are distinct, their column-maximum Z_H (i.e., composite reflectivity) and low-level Z_H values can be similar in magnitude. For example, $Z_H = 40$ dBZ at 3 km may just as easily be considered convective as stratiform. Thus, in order to avoid the obvious limitations of a Z_H threshold-based convective-stratiform classification at a single altitude, the SL3D algorithm uses the depth of radar echo (i.e., continuous vertical column of Z_H), its maximum altitude (i.e., echo top), and its intensity relative to the surrounding echo to distinguish between convective and stratiform regions. The SL3D convection classification utilizes height information to identify deep convection by locating enhanced regions of Z_H that extend above the melting layer. These vertical columns of enhanced Z_H are effectively used as a diagnostic, or proxy, for convective motion. Only strong vertical motions can loft large particles high enough to be able to generate the associated continuous high Z_H in the vertical dimension, while the enhanced Z_H of stratiform precipitation is confined to the melting level and below.

The SL3D convective classification is internally partitioned into three steps to better identify convection of varying extent and intensity. Radar echo in each grid square that meets any of the following three criteria is labeled as convection: 1) Z_H = 25-dBZ echo top extending above 10 km, 2) horizontal layer ”peakedness” that is the maximum of either 4.0 dBZ or $10.0 - Z_H^2/337.5$ dBZ, or 3) $Z_H \geq 45$ dBZ at any altitude above the melting level. Each of these three criteria is discussed in more detail below.

Criterion 1 uses $Z_H = 25$ dBZ, but $Z_H \geq 30$ dBZ is frequently used to define convection and/or the convective extent (e.g., DeMott and Rutledge 1998). While the SL3D convective classification is relatively insensitive to the choice of $Z_H = 30$ dBZ or $Z_H = 25$ dBZ, we use the slightly lower $Z_H = 25$ dBZ to better capture weaker convection, where the $Z_H = 30$ dBZ boundary may be present just below 10 km. For criterion 2, the horizontal peakedness of each grid point is evaluated to better locate shallow and midlevel convection that may be embedded within a deep or expansive stratiform cloud. Building upon the SHY algorithm, peakedness is considered to be the difference between the Z_H of the grid point being evaluated and the median Z_H of a 12-km radius around the point. The peakedness of a grid point is determined at each height where radar echo is present in the lowest 9 km of the radar volume. A grid point is labeled as convection if at least 50% of the vertical column peakedness surpasses a threshold that varies with Z_H (i.e., 50% of the vertical radar echo surpasses the peakedness threshold). This variable threshold approach is equivalent to that outlined in SHY, but we use a slightly altered relationship: the higher of 4.0 dBZ or $10.0 - Z_H^2/337.5$ dBZ. This alteration is based on both constant peakedness thresholds used in studies prior to SHY (e.g., Churchill and Houze 1984) and our intended avoidance of an absolute reflectivity limit for convective/stratiform discrimination when the variable peakedness threshold reaches zero. Finally, in criterion 3, the 45-dBZ threshold is generally considered to be indicative of the transition point from graupel to small hail at S band and is only routinely generated by riming in convective updrafts (e.g., Straka et al. 2000). No Z_H associated with the stratiform region should approach this threshold above the melting level, but it may approach or exceed 45 dBZ below the melting level via microphysical or dynamical processes.

Once convective regions are identified using the three criteria outlined above, we apply two quality control techniques that modify the classification. Any single convective grid point that is adjacent only to nonconvective grid points is removed, as it is expected to be false or inconclusive based on the classification criteria. Once the single-point classifications are removed, any grid points immediately adjacent to remaining convective echo are also classified as convective if their column-maximum $Z_H \geq 25$ dBZ. The reason for reclassifying the adjacent grid squares and expanding the convective classification is similar to that of the convective radius step in SHY. Grid squares that are marginally below the peakedness threshold but are on the periphery of identified convective regions are likely resultant from the same convective processes.

Grid points that do not meet the convective criteria undergo possible stratiform classification. The stratiform classification in SL3D is split into two mutually exclusive categories: 1) precipitating stratiform and 2) nonprecipitating stratiform. While vertical velocities in stratiform regions are typically an order of magnitude smaller than those in convection, considerable differences in vertical velocities between precipitating and nonprecipitating stratiform clouds have also been documented. For instance, Schumacher et al. (2015) found that mean vertical velocities in the tropics from the near surface to 10 km ranged from −0.1 to 0.2 m s^{-1} for stratiform and from 0.1 to 0.9 m s^{-1} for convection. The full spectra of vertical velocity measurements varied from about −2 to 2 m s^{-1} for stratiform and from −5 to 18 m s^{-1} for convection. For nonprecipitating cloud (their transitional anvil), the mean vertical velocities were weaker than stratiform and varied from −0.05 to 0.05 m s^{-1}, with minima and maxima ranging from about −1.25 to 1.5 m s^{-1} (Schumacher et al. 2015). The nonprecipitating stratiform region encompasses the transition between precipitating stratiform and ice-only anvil, where some stratiform growth (i.e., aggregation) has occurred but does not lead to precipitation. Ideally, regions categorized as precipitating stratiform include only those observations with nonconvective precipitation at the surface. However, since radar coverage is limited near the surface, data at 3 km are used to draw the primary distinction between precipitating and nonprecipitating echoes. The 3-km height is the lowest altitude with near-uniform coverage in the NEXRAD WSR-88D network. When available, data below 3 km are used to identify additional regions of weak precipitation. The 3-km analysis level is also used in the SHY algorithm for comparisons with SL3D in section 5 below.

Precipitating stratiform is defined as that with $Z_H \geq 20$ dBZ at 3 km or $Z_H < 20$ dBZ present at 3 km when $Z_H \geq 10$ dBZ is present at one or more of the lower-altitude levels (1 or 2 km). These Z_H thresholds are similar to those used in other studies, such as Feng et al. (2011) and Schumacher et al. (2015), which generally use $Z_H \geq 10$ dBZ to identify stratiform precipitation at lower altitudes. The higher $Z_H = 20$ dBZ threshold at 3 km relative to the aforementioned studies was determined by analyzing several dozen cases, and is in place to ensure precipitation is reaching the surface. On its own, $Z_H = 10$ dBZ at 3 km is not a reliable indicator of precipitation. Nonprecipitating stratiform encompasses any echo that extends to altitudes at or below the melting level, but does not meet the requirements for precipitation outlined above.

As briefly outlined above, we specify the melting-level altitude in SL3D to assist with echo classification. While some unique radar features can be used to help identify stratiform regions (e.g., Z_H bright band or its commonly used dual-polarization counterpart, a ρ_{HV} reduction), we do not employ such techniques in SL3D. These techniques are not used because 1) not all stratiform regions contain such signatures and some dual-polarization indicators of stratiform rain can also be found in deep convection (e.g., see Houze 1993, 1997; Steiner et al. 1995; Schumacher et al. 2015), 2) there is insufficient vertical resolution in the radar dataset used in this study for resolving such features, and 3) these techniques would include unnecessary limitations to the classification based on the availability of dual-polarization variables, which are only present in the WSR-88D data since late 2012. Fundamentally, the goal of the SL3D algorithm is to be applicable regardless of radar polarization, intrinsic vertical resolution, and region or large-scale environment.

b. Anvil

In previous studies, anvil regions have commonly been separated into modes thought to be representative of unique physical and/or dynamic regimes. For example, Frederick and Schumacher (2008) stratified anvil into mixed-phase and ice-only cloud due to important differences in radiative properties between the two categories. The SL3D anvil classification is designed to identify nonprecipitating ice-only cloud above the melting level resulting from convective detrainment in the upper troposphere (mixed-phase nonprecipitating clouds are categorized as nonprecipitating stratiform). To accomplish this, we identify regions as anvil if radar echo ($Z_H \geq 0\,\mathrm{dB}Z$) is only present above an altitude of 5 km, which is typically the maximum height of the melting level and is similar to the approach of Feng et al. (2011) and Carletta et al. (2016). Requiring the 5-km threshold prevents potential misclassifications of echo in environments where the melting-level altitude approaches the surface and the likelihood of the anvil precipitating increases.

c. Convective updraft

Following the convection, stratiform, and anvil classification, radar echo is evaluated to determine whether or not signatures indicative of strong convective updrafts are present. To identify convective updrafts, the SL3D algorithm searches for three well-known radar signatures: 1) weak-echo regions [WERs; bounded or unbounded, e.g., Browning and Donaldson (1963); Musil et al. (1986); Calhoun et al. (2013)], 2) Z_{DR} columns (e.g., Caylor and Illingworth 1987; Illingworth 1988; Bringi et al. 1991; Conway and Zrnić 1993; Ryzhkov et al. 1994; Brandes et al. 1995; Loney et al. 2002; Scharfenberg et al. 2005; Kumjian and Ryzhkov 2008; Kumjian et al. 2014), and 3) K_{DP} columns (e.g., Zrnić et al. 2001; Loney et al. 2002; Kumjian and Ryzhkov 2008; Van Lier-Walqui et al. 2016). WERs are elements of a convective storm with relatively low Z_H values at lower altitudes that are at least partially bounded horizontally and above by relatively high Z_H values. Such WERs have been shown to represent a lack of large, precipitable hydrometeors due to strong (rapid) ascent of developing particles in the updraft of a convective storm. From a radar detectability perspective, the most easily identifiable WERs are bounded by regions of high reflectivity. Bounded WERs are generally indicative of a strong updraft embedded within a strongly sheared environment, and are commonly found in supercell convection (e.g., Markowski 2002). The SL3D algorithm identifies WERs in the altitude layer below 7 km where 1) the vertical Z_H gradient $\geq 8\,\mathrm{dB}Z\,\mathrm{km}^{-1}$ in a grid volume, 2) echo is present in at least six of the eight horizontally adjacent grid volumes, and 3) column-maximum $Z_H \geq 40\,\mathrm{dB}Z$. Although some storms contain WERs extending to altitudes above 7 km, the altitude limitation and neighborhood check are necessary to limit overidentification of updraft regions in vertically tilted convection.

For radar composites that include the full suite of polarimetric variables, updraft classifications also include Z_{DR} and K_{DP} columns. The Z_{DR} and K_{DP} columns are regions of enhanced positive values (generally ≥ 1 dB and $\geq 0.5\,\mathrm{dB\,km}^{-1}$, respectively) extending to altitudes above the environmental freezing level. The columns represent deep lofting of liquid hydrometeors within a convective updraft. Since Z_{DR} is a size-weighted measure of particle shape, the Z_{DR} columns identify updrafts capable of lofting large raindrops above the freezing level (which may also include small hail). The K_{DP} columns, on the other hand, indicate updrafts that have lofted large concentrations of moderately sized (2–4 mm) raindrops above the freezing level (e.g., Loney et al. 2002). Van Lier-Walqui et al. (2016) found that K_{DP} columns are not only a good indicator of the presence of an updraft, but changes in the volume of a K_{DP} column are correlated to changes in the updraft mass flux.

Snyder et al. (2015) have recently developed an algorithm for objectively identifying Z_{DR} columns in single-radar observations. In short, their algorithm identifies a column of $Z_{DR} \geq 1$ dB at altitudes above the freezing level, which is consistent with the approach we have designed independently here using a slightly higher Z_{DR} threshold. In the SL3D algorithm, the Z_{DR} and K_{DP} columns are identified as those with $Z_{DR} \geq 1.5$ dB or $K_{DP} \geq 0.5^\circ\,\mathrm{km}^{-1}$ extending at least 1 km above the freezing level. The slightly higher threshold of Z_{DR} used here compared to Snyder et al. (2015) accounts for calibration issues and potential broadening of polarimetric signatures when data are composited from multiple radars. The K_{DP} threshold is set to discriminate between high concentrations of raindrops above the melting level and snow (which typically occupies a K_{DP} range from -0.5° to $0.5^\circ\,\mathrm{km}^{-1}$). In addition, only echo with $Z_H \geq 15\,\mathrm{dB}Z$ is considered for Z_{DR} column detection, and echo with $Z_H \geq 30\,\mathrm{dB}Z$ for K_{DP} column detection in order to avoid

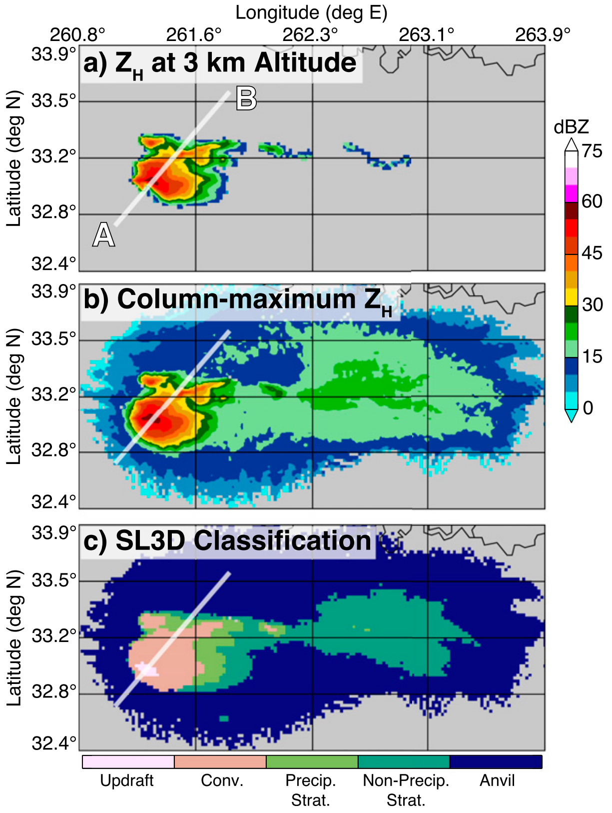

FIG. 1. Maps of (a) Z_H at 3-km altitude, (b) column-maximum Z_H, and (c) SL3D classification for a supercell located in northeast TX at 0055 UTC 18 May 2013. The thick line labeled A–B in (a) and shown in each map shows the location of the vertical cross sections in Fig. 2.

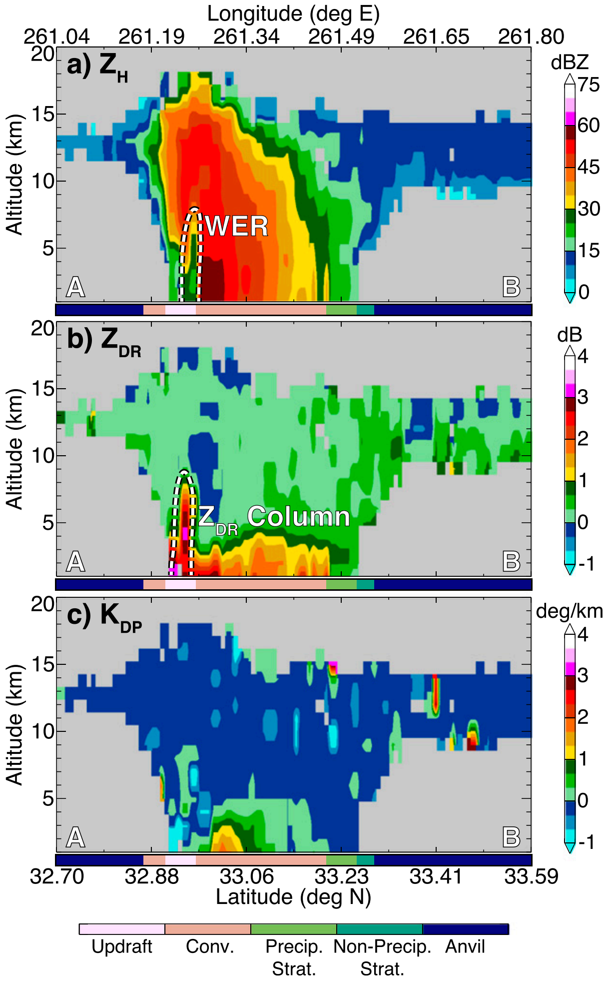

FIG. 2. Vertical cross sections of (a) Z_H, (b) Z_{DR}, and (c) K_{DP} following the thick line in Fig. 1, from A (left) to B (right). The thick colored line at the base of each cross section shows the corresponding SL3D classification.

common biases (noise) along the periphery of radar echoes.

SL3D updrafts are identified by locating Z_{DR} and K_{DP} columns in grid volumes that lie within 12 km of any previously identified convective grid point. The 12-km radius was chosen to enable identification of updrafts that may be displaced relative to the intense precipitation column, especially in vertically tilted storms. Based on the authors' experience, this distance is also a common scale of horizontal separation between convective cells in organized convective systems. Therefore, this radius is viewed as an upper limit for neighborhood searching, since expanding the radius to larger values may commonly enable false identifications in nonconvective rain regions.

Finally, following identification of WERs, Z_{DR} columns, and K_{DP} columns, we apply a single quality-control step. Similar to the approach for convective classification, any grid point identified as a convective updraft that is horizontally surrounded by nonconvective updraft echoes (i.e., single-point classifications) is removed and the prior classification restored.

4. Example SL3D classifications and convective updraft validation

To demonstrate the application of the SL3D classification, we show a simple dual-polarization case in Fig. 1 that contains a large supercell storm in north Texas at 0055 UTC 18 May 2013. The melting level for this case is ~4.75 km. Figure 1a shows a 3-km constant-altitude map of Z_H. The supercell reaches a maximum of Z_H near 60 dBZ and contains a well-defined hook echo at 3 km in the southwest quadrant of the storm. An extensive anvil region is visible through contrasting regions of echo in the 3-km and column-maximum Z_H maps (Figs. 1a and 1b) and in the corresponding SL3D classification (Fig. 1c). There are three smaller and weaker convective storms to the north and northeast of the supercell.

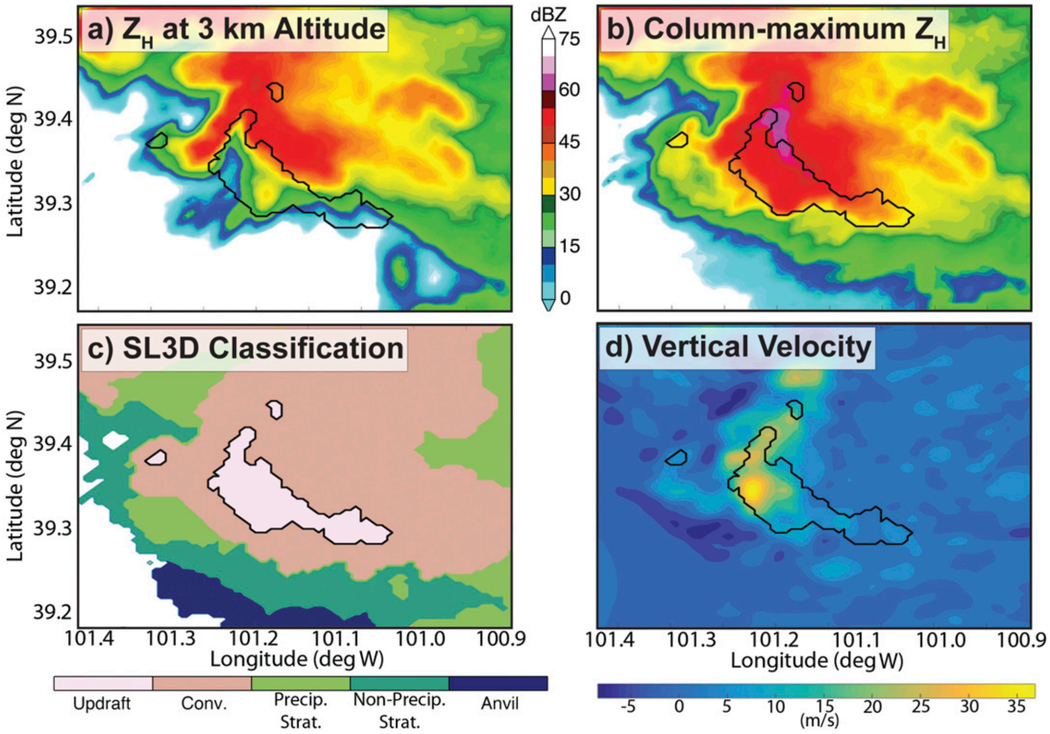

FIG. 3. Maps of (a) Z_H at 3-km altitude, (b) column-maximum Z_H, (c) the SL3D classification, and (d) dual-Doppler-derived mean vertical velocity in the vertical column from a storm observed during STEPS at 0030 UTC 30 Jun 2000. The black lines denote the SL3D updraft classifications using WER identification alone.

The SL3D classification shows that the precipitating portion of the supercell is largely identified as convection, with a broad convective updraft near the location of the hook echo. To determine what physical characteristics are contributing to the SL3D classification of the supercell, we present a vertical cross section of the polarimetric variables in Fig. 2 along a path that bisects the storm's hook echo and updraft region (the A–B line in each map in Fig. 1). The vertical sections reveal that both a deep (up to 8 km in altitude) bounded WER and Z_{DR} column contribute to the updraft classification, while there is no significant K_{DP} column signature. In addition, the supercell reaches altitudes up to 18 km (consistent with its convective classification) and SL3D convective regions correspond directly to vertically erect volumes of high Z_H. There is no apparent bright band in the Z_H section (Fig. 2a) and likewise little echo classified as stratiform rain by SL3D. Both forward and rear ice-only anvils are observed to be extending away from the storm between ~9 and 15 km and they are captured well by SL3D.

While the example using WSR-88D observations in Figs. 1 and 2 is encouraging, validation of the performance of the echo-based updraft algorithm is desired to establish confidence in its use. To achieve such validation, we include examples of SL3D application to two multi-Doppler radar cases, which provide measurements of the three-dimensional wind fields within storms. The vertical velocities were retrieved using variational integration of the continuity equation (O'Brien 1970). Figure 3 presents application of the SL3D algorithm to a supercell storm at 0030 UTC 30 June 2000 that was observed during the Severe Thunderstorm Electrification and Precipitation Study (STEPS; Lang and Rutledge 2002; Lang et al. 2004). Since this case includes only single-polarization radar observations (i.e., Z_H), updraft identification in SL3D comes from the WER algorithm alone. The WER identified in SL3D encompasses a large region of the storm extending southeast from the hook echo located along the southwestern flank of the storm at 3 km (Fig. 3a). In addition, the WER coincides with the highest vertical velocities observed in the dual-Doppler wind field (i.e., the updraft; see Fig. 3d). Despite the success of the SL3D identification, there are a couple of points worth noting: 1) while the main updraft region is identified, another region of enhanced vertical velocity to the north is not identified by SL3D because of the absence of a WER, and 2) the WER identified in SL3D extends to regions in the southeastern portion of the storm that have weak and/or marginal upward motion.

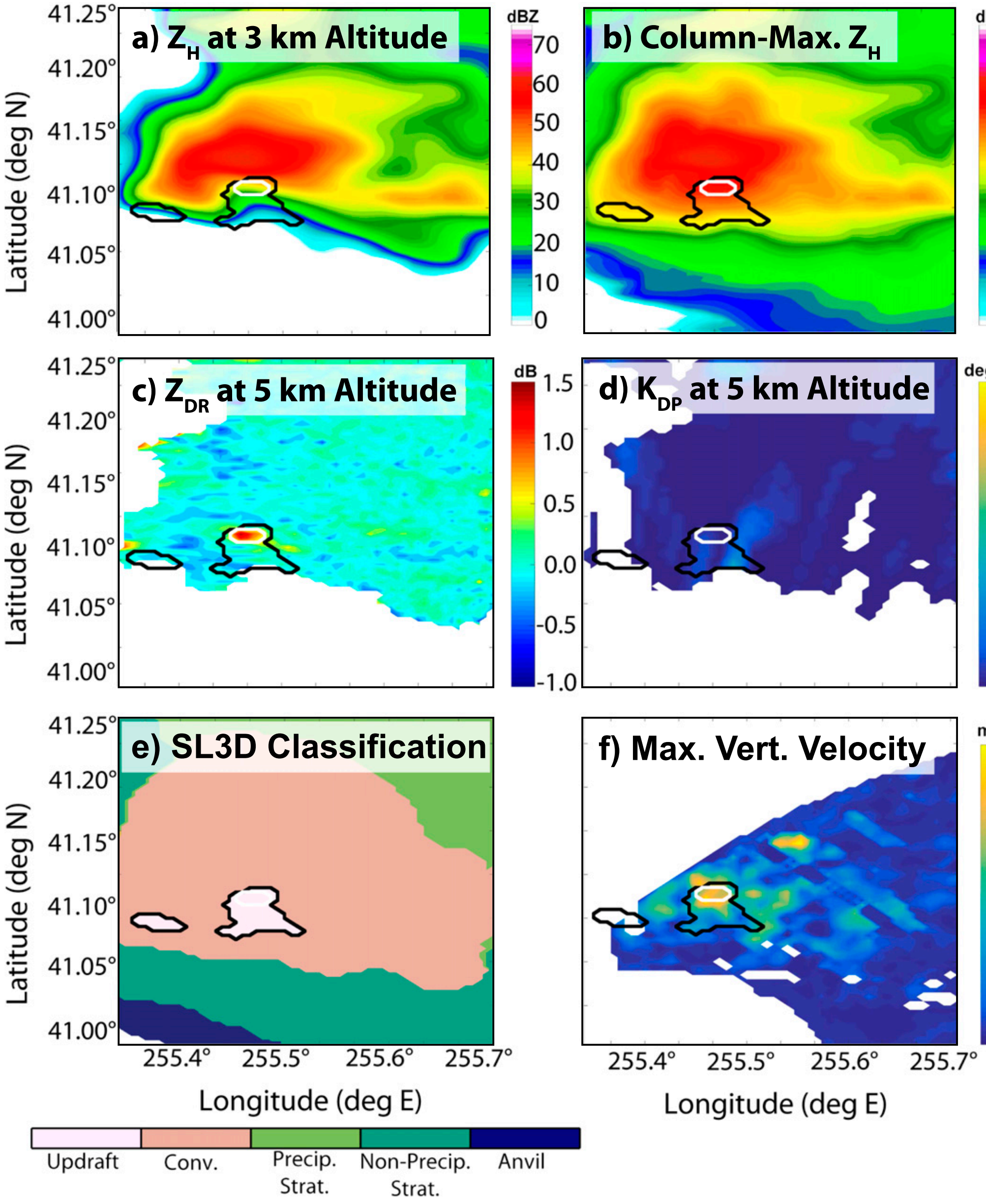

FIG. 4. Maps of (a) Z_H at 3-km altitude, (b) column-maximum Z_H, (c) Z_{DR} at 5-km altitude, (d) K_{DP} at 5-km altitude, (e) the SL3D classification, and (f) the maximum dual-Doppler-derived vertical velocity at 2230 UTC 6 Jun 2012. The black lines denote the SL3D updraft classifications using WER identification alone and the white lines denote the SL3D updraft classifications using polarimetric variables alone.

A second validation case is provided in Fig. 4. For this case, dual-Doppler radar observations are taken from a storm in northeast Colorado (Basarab et al. 2015; Basarab 2015) observed at 2230 UTC 6 June 2012 during the Deep Convective Clouds and Chemistry (DC3) experiment (Barth et al. 2015). In contrast to the STEPS storm, this DC3 case includes dual-polarization observations that allow for validation of the entire three-step updraft identification algorithm in SL3D. For this case, the updraft identified in both SL3D and the Doppler wind field is displaced to the south of the most intense precipitation (Figs. 4a and 4f). Although the updraft region is displaced, the updraft location in the dual-Doppler wind field and SL3D classification are nearly coincident. The WER is once again visible by comparing the 3-km and column-maximum Z_H results (Figs. 4a and 4b, respectively), where the SL3D-identified WER is denoted by the black line. In this case, no significant K_{DP}

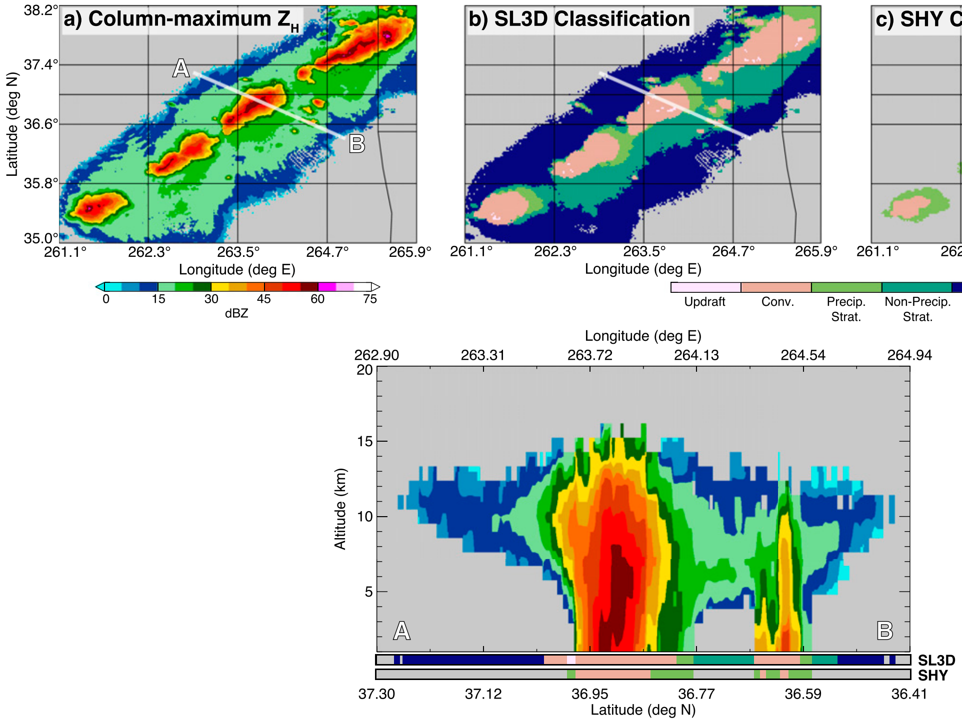

FIG. 5. Maps of (a) column-maximum Z_H, (b) SL3D classification, (c) SHY classification, and (bottom) a vertical cross section of Z_H following the thick line labeled A–B in (a) for a collection of deep quasi-linear convective storms over OK and southeast KS at 0125 UTC 14 May 2009. The thick colored lines at the base of the cross section show the corresponding SL3D and SHY classifications.

(Fig. 4d) columns are present, so the Z_{DR} column detection element of SL3D is the primary source of the dual-polarization updraft classification step (white line), as depicted by the regions of high Z_{DR} at ~1 km above the melting level or a true altitude of 5 km (Fig. 4b).

5. Comparisons of SL3D with traditional methods

As outlined in the introduction, traditional radar echo classification methods like the SHY algorithm are designed for precipitation estimation and use a single low-altitude map of Z_H to identify convection and stratiform rain. The SL3D algorithm incorporates the three-dimensional information of the radar observations to build upon such classifications when information in the vertical is needed. It is therefore important to evaluate the success of this three-dimensional approach and its performance relative to the SHY method in order to determine the impacts on the classification. We show several comparisons of the SL3D and SHY classifications in this section for storms with varying organizational structures, large-scale forcings, and geographic locations. To produce comparable classifications, the SHY algorithm is applied to Z_H fields at 3 km in each case. Based on the analysis of Feng et al. (2011) using multiradar composites, we use a Z_H threshold of 43 dBZ for the first SHY step, a background radius of 6 km for the second step, and a convective radius of up to 3 km for the final step. Echo below 10 dBZ is considered to be too weak for precipitation and is not included in the stratiform classification.

Figures 5a–c show maps of column-maximum Z_H, the SL3D classification, and the SHY classification, respectively, for a collection of deep quasi-linear convective storms primarily within Oklahoma and southeast Kansas at 0125 UTC 14 May 2009. The melting level for this case is ~4.5 km. Comparison of the SL3D and SHY classifications shows that the outermost boundaries of the precipitating regions are very similar, and any differences in the overall scale of precipitating regions for this case are arguably negligible. However, comparison of the SL3D and SHY classifications shows that convective regions are larger in the SL3D classification. This difference in convective classification is a direct result of the dependence of the SL3D algorithm on the vertical extent of a storm rather than a low-altitude Z_H threshold and is common across a large number of additional cases. When the SHY algorithm is applied at an altitude of 3 km, it identifies the largest Z_H values as convective, and expands the convective classification using the two-step radii thresholds. However, the SL3D method identifies a much larger convective region based on the

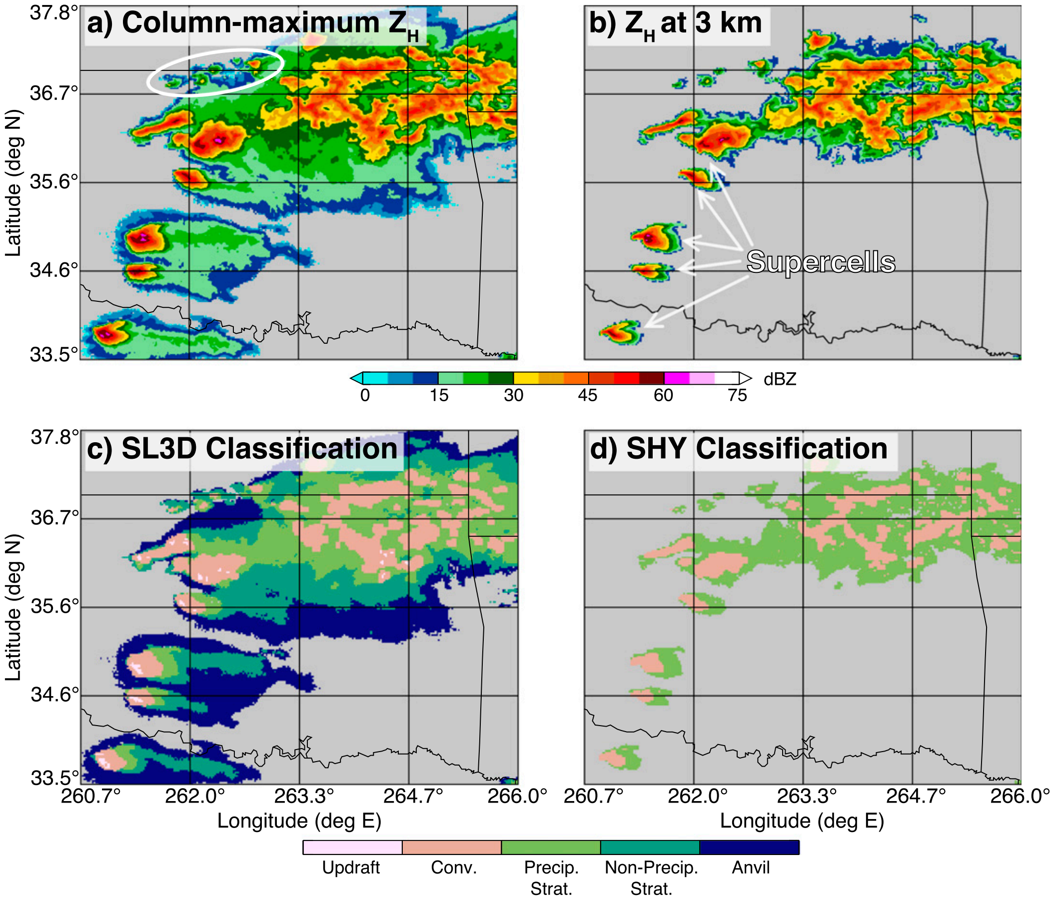

FIG. 6. Maps of (a) column-maximum Z_H, (b) Z_H at 3-km altitude, (c) SL3D classification, and (d) SHY classification for a collection of supercell storms and an MCS over OK at 2325 UTC 23 May 2011. The white ellipse in (a) encloses weaker convection that is discussed in the text.

vertical extent of the storm, regardless of the magnitude of Z_H at lower levels. These differences in convective classification are demonstrated further in the vertical cross section labeled A–B in Fig. 5a. The largest convective cell in the cross section has a broader horizontal extent of high reflectivity (≥30 dBZ) aloft than near the surface, which is responsible for the broader SL3D convective classification compared to SHY. For the two smaller convective cells in the cross section, both SL3D and SHY identify the largest Z_H values as convective, but the SHY algorithm underrepresents the horizontal extent of the storms, as evidenced by the Z_H columns.

Figure 6 shows application of the SL3D algorithm to a case containing multiple discrete supercell storms and a mesoscale convective system (MCS) over central and northeastern Oklahoma, respectively, at 2325 UTC 23 May 2011. The melting level for this case is ~4.25 km. This case demonstrates the performance of the SL3D classification for a wide variety of convective organizations and intensities. Only single-polarization observations are available, such that updrafts are classified using WER identification alone. Both SL3D and SHY produce reasonable convective classifications within the MCS, again with noticeably larger convective regions in the SL3D classification. The differences in the scales of convective classifications between SL3D and SHY are largest in the supercell storms, which is a reflection of the dependence of SL3D on the depth of the intense reflectivity column. For the WER-only updraft classification in SL3D, this case demonstrates that unless the convection is sufficiently intense, few, if any, updraft regions are identified using the WER method alone. In particular, each supercell has a clearly defined updraft, demonstrating the robustness of the WER classification method in supercell storms, which (as discussed in section 3c) typically contain large bounded WERs. The MCS in the northeastern portion of the domain, however, shows little to no area classified as convective updraft.

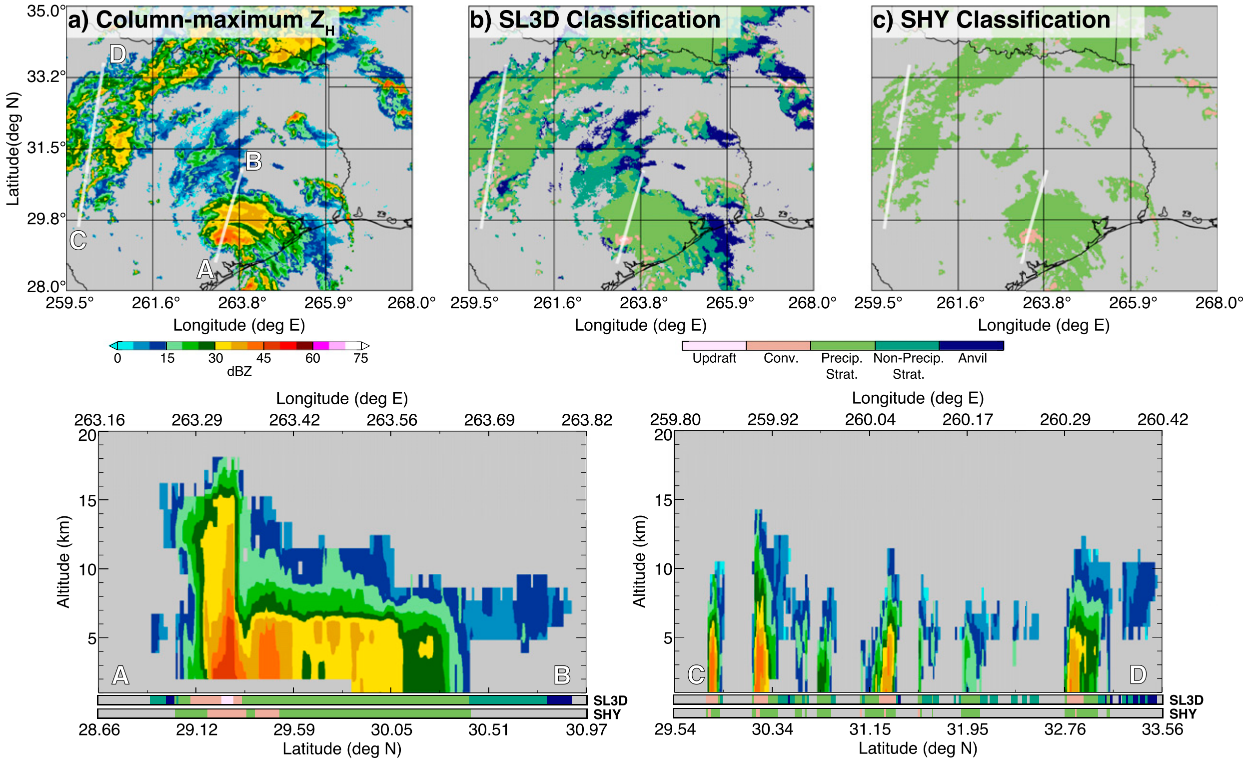

FIG. 7. Maps of (a) column-maximum Z_H, (b) SL3D classification, (c) SHY classification, and (bottom) vertical cross sections of Z_H following the thick lines labeled A–B and C–D in (a) for Tropical Storm Bill in southeast TX and additional nearby precipitation in AR, LA, OK, and TX at 0000 UTC 17 Jun 2015. The thick colored lines at the base of each cross section show the corresponding SL3D and SHY classifications.

The cases presented thus far are largely limited to intense and/or extreme storms located in the U.S. Great Plains. To demonstrate the success of SL3D in other regions and environments, we include three additional cases here and a fourth in section 6 below. First, Fig. 7 shows observations centered over southeast Texas during the landfall of Tropical Storm Bill at 0000 UTC 17 June 2015. Additional weaker convection and stratiform rain is included in the northwestern portion of the domain and moderately intense convection in the eastern portion of the domain. The melting level for this case is ~4.75 km; however, a pronounced increase in the melting-level height is noted by the height of the bright band within Tropical Storm Bill (line A–B; Fig. 7). While differences similar to those outlined in previous cases can be observed here, we focus our attention on differences within the tropical storm and in the broad area of weak convection surrounded by stratiform rain in the northwest portion of the domain. Specifically, the vertical cross section labeled A–B in Fig. 7a bisects Tropical Storm Bill, while the cross section labeled C–D bisects the weaker convection.

For Tropical Storm Bill, a deep convective tower is observed to be reaching altitudes in excess of 17 km near the center of the storm, followed by a large region of weak-to-moderate stratiform rain radially outward. Both the SL3D and SHY classifications correctly identify the convective region near the center of the storm, with the SL3D convective classification extending farther toward the center. The displacement of the SL3D classification relative to that from SHY corresponds to the extension of higher reflectivity aloft, capturing the weaker precipitation just below the high-reflectivity column. Radially outward from the convective region, however, is a region with larger differences between the SL3D and SHY classifications. Namely, there is a region of intense stratiform rain classified by SHY as convective. Though overrepresentation of convection by the SHY algorithm is rare, such false classification is due to the absolute Z_H threshold used for convective precipitation in the SHY algorithm (i.e., 43 dBZ).

Additional differences between the SL3D and SHY classifications are observed in the cross section through the weaker convection in Fig. 7 (labeled C–D). This cross section demonstrates the SL3D classification capturing

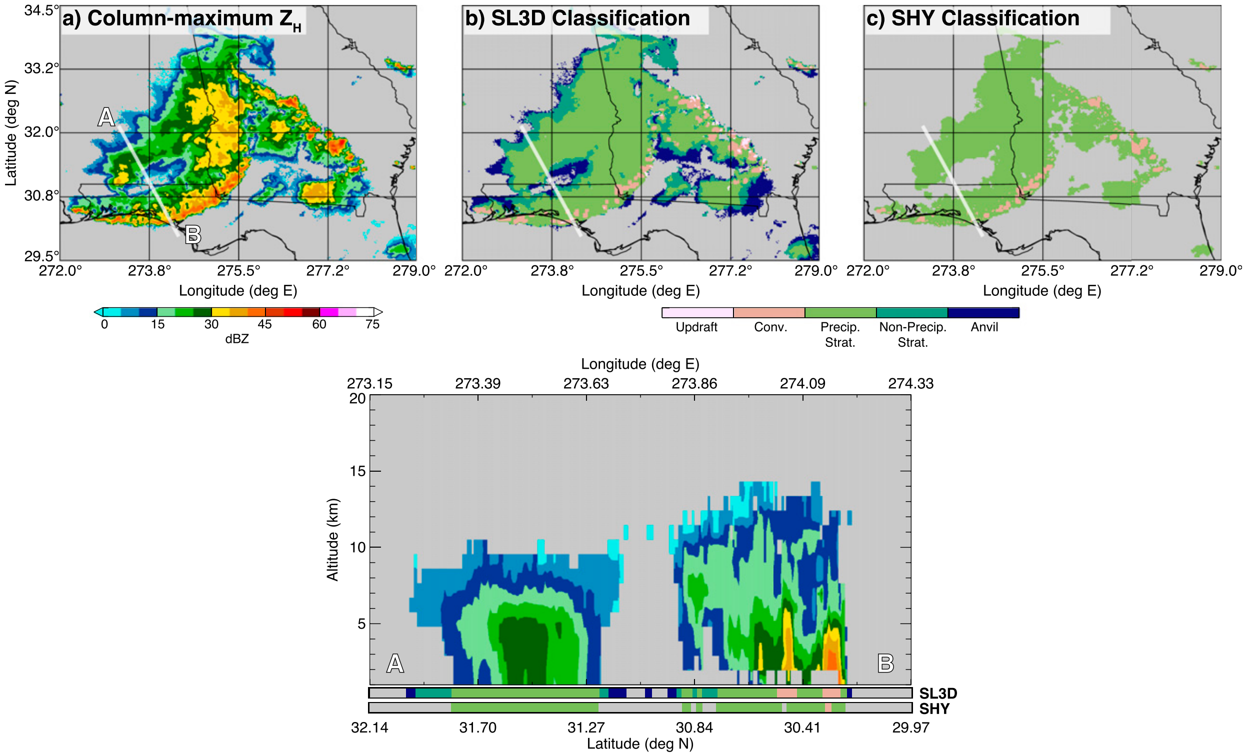

FIG. 8. Maps of (a) column-maximum Z_H, (b) SL3D classification, (c) SHY classification, and (bottom) a vertical cross section of Z_H following the thick line labeled A–B for an MCS located over AL, FL, and GA at 0000 UTC 24 Jul 2013. The thick colored lines at the base of the cross section show the corresponding SL3D and SHY classifications.

the horizontal extent of higher reflectivity in the weaker storms while the SHY algorithm classifies smaller regions that appear to be primarily limited to exceedances of the 43-dBZ Z_H threshold at 3 km. Leveraging of additional vertical information in the SL3D algorithm enables improved classification of weak convection for both this case and the 23 May 2011 case (see Fig. 6a, white ellipse). This difference highlights that SHY was primarily designed for surface precipitation estimation and is not focused on convective motions aloft.

Further examples of improvements in the classification of weaker convection can be found in storms from the Southeast and Northeast regions of the United States (Figs. 8 and 9, respectively). The melting level for the Southeast case is ~4.5 km and for the Northeast case it is ~4.25 km. For the Southeast case, there are two lines of convection: one translating northwest to southeast across the Florida panhandle and the other translating southwest to northeast across central Georgia. For both convective lines, SL3D convective classifications are both more numerous and slightly broader in horizontal extent. We present a cross section in Fig. 8 through one of the convective regions that is broad in the SL3D classification and marginally present in the SHY classification. In this cross section, two weak-to-moderate convective cells are apparent on the southern end of the storm and reach altitudes at and slightly above the melting level. While SL3D identifies both of these convective regions well, SHY misses the deeper of the two, which has lower column-maximum Z_H. Apart from these differences in the convective regions, the two classifications are similar. For the northeast case, there is a large MCS in the central and northeastern portions of the domain and weaker discrete convection in the western portion of the domain. The SL3D and SHY classifications are similar in the MCS where convection is deeper and Z_H is more intense, but the results differ considerably in the weaker convection to the west. The vertical cross section in Fig. 9 bisects both the weak discrete convection and the deeper convection of the MCS. Once again, the largest differences between the SL3D and SHY classifications are observed in the weaker, shallower storms, which are marginally captured in the SHY algorithm.

6. Importance of the polarimetric updraft classification

As outlined in section 3c and demonstrated using multiple cases in this study, convective updraft identification using single-polarization radar observations with the

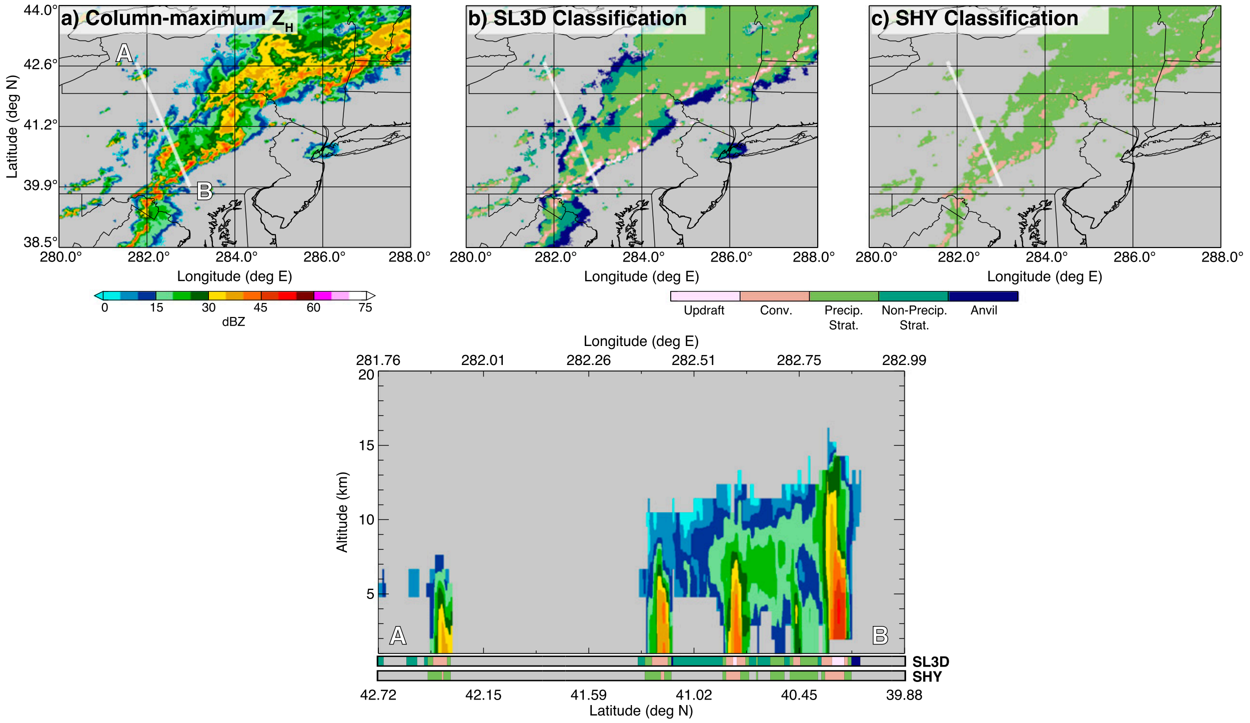

FIG. 9. As in Fig. 8, but for scattered weak convection and an MCS located primarily over NY and PA at 2300 UTC 25 Jun 2014.

SL3D algorithm is limited to the existence of WERs in Z_H. Furthermore, while WERs are a commonly observed radar characteristic of supercell storms (e.g., Markowski and Richardson 2010), such as in Fig. 6, many storms do not contain discernible WERs. This limitation means that updraft regions within the majority of convection observed by single-polarization radar cannot be detected with this method. Fortunately, polarimetric radar observations enable updraft identification within most convective regions without WERs through the detection of raindrops lofted to altitudes above the environmental freezing level (Z_{DR} and K_{DP} columns). However, despite representing similar microphysical characteristics, the Z_{DR} and K_{DP} columns do not always coexist (e.g., Loney et al. 2002). Similarly, both Z_{DR} and K_{DP} vary differently with varying sizes and concentrations of hail and hail–rain mixtures. For example, in hail–rain mixtures, the Z_{DR} signal may be dominated by the presence of large, tumbling hail. Because of the smaller dielectric constant of ice, lower concentration of hailstones, and spherical shape of hailstones (Balakrishnan and Zrnić 1990), K_{DP} is affected little by hail. Thus, in order to enable classification of as many convective updrafts as possible, it is critical to use Z_{DR} columns, K_{DP} columns, and WERs for updraft classification.

Figures 10 and 11 demonstrate the importance of identifying both Z_{DR} and K_{DP} columns for a leading-line trailing-stratiform MCS over northern Indiana and Ohio at 0330 UTC 13 June 2013. The melting level for this case is ~4.5 km. Figures 10a–c show maps of column-maximum Z_H, Z_{DR} at 5-km altitude, and K_{DP} at 5-km altitude, respectively, centered on the leading convective line. The 5-km-altitude level for the polarimetric variables is chosen since it lies immediately above the environmental melting (freezing) level. The convective line is clearly visible as a narrow region of large Z_H (>40 dBZ) in the column-maximum map, with corresponding updraft regions shown as distinct maxima in the polarimetric variables at 5 km. However, comparison of the Z_{DR} and K_{DP} maps reveals that the largest values of each variable generally correspond to relatively low values in the other, especially in the northeastern elements of the convective line. This behavior suggests that Z_{DR} columns are more prevalent in southwestern elements of the convective line and K_{DP} columns are more prevalent in the northeastern portion. The spatial offsets are further demonstrated in the vertical cross sections in Figs. 11a–c, taken along path A–B in Fig. 10, which bisect a storm with sparse Z_{DR} column detection and prevalent K_{DP} column detection. These cross sections show that while no WERs or deep Z_{DR} columns are evident within the storm, a deep K_{DP} column extending up to ~3 km above the melting level enables detection of the updraft in this case.

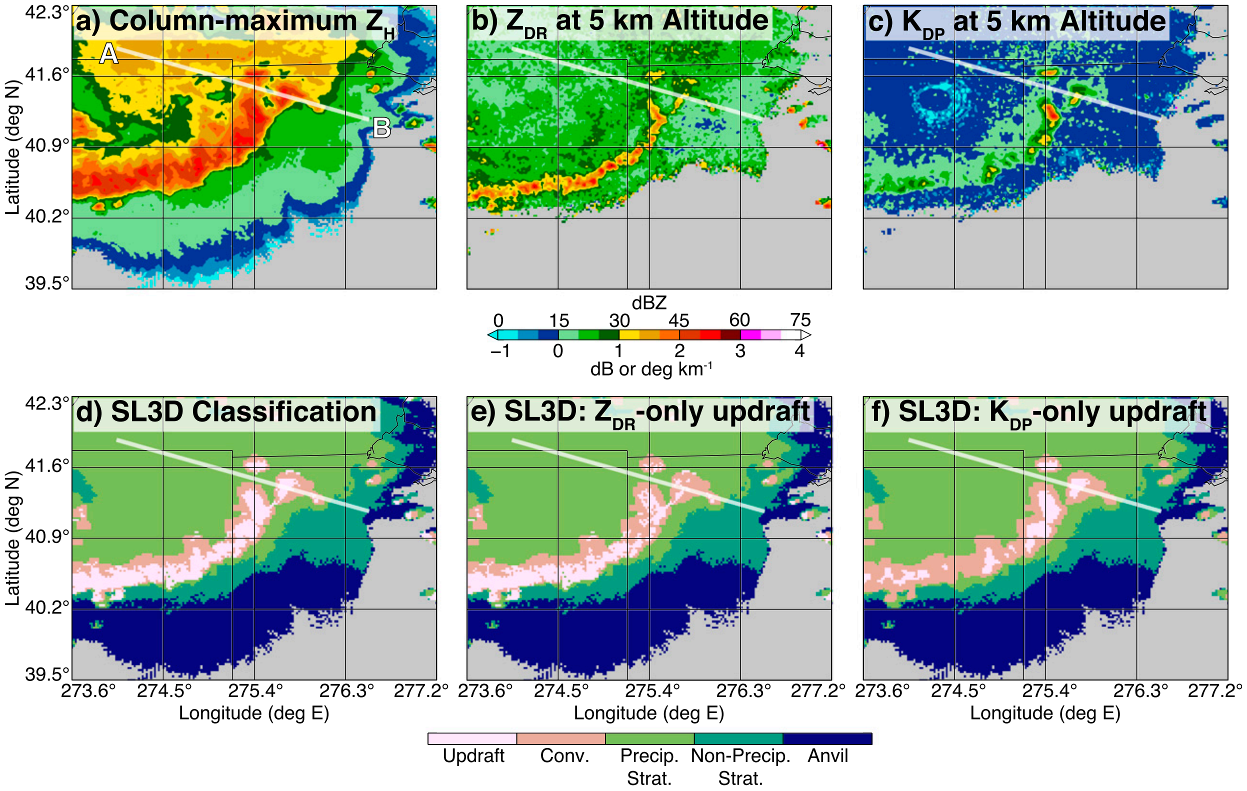

FIG. 10. Maps of (a) column-maximum Z_{H}, (b) Z_{DR} at 5-km altitude, (c) K_{DP} at 5-km altitude, (d) SL3D classification, (e) SL3D classification with Z_{DR}-only updraft classification, and (f) SL3D classification with K_{DP}-only updraft classification for an MCS located in northern IN and OH at 0330 UTC 13 Jun 2013. The thick lines on each map show the locations of the vertical cross sections in Fig. 11.

7. Limitations of the SL3D algorithm

Although we have presented several successful applications of the SL3D algorithm, there are some limitations of the method worth discussing here. While the WER updraft classification performs well in strong supercell storms and is able to identify the core updraft region (e.g., Fig. 3), more quantitative validation is required. Additionally, there are cases where false WER-based updraft classifications are revealed in the SL3D classification. Such false WERs are typically associated with deep convection containing narrow regions of precipitation, leading to updraft classifications on both upstream and downstream sides of the storm. In reality, most updrafts are limited in space to one side of a storm (e.g., Jorgensen et al. 1997; Lang and Rutledge 2008; and Figs. 3 and 4 here). Examples of this error can be seen for the 14 May 2009 case in Fig. 5. It should be noted, however, that such WER errors typically account for $\ll$1% of the total classified area (determined by analyzing updraft classifications in several additional cases not shown here). Thus, we expect false WER identifications to be negligible in most (if not all) cases.

While the convective classification in SL3D performs well in most cases, there are times where some stratiform rain is falsely classified as convection. The thresholds used in the convective classification here were chosen in order to minimize such errors using many case studies of the NEXRAD WSR-88D composite observations. These errors depend strongly on the intensity of stratiform rain and the melting-level altitude (which may be modified significantly within a storm). Future studies are needed to examine the probability of detection and false alarm rate of the convective classification for weak convection.

Finally, there are important limitations of the SL3D algorithm related to the characteristics of the radar dataset it is applied to. Since the SL3D classifications require substantial vertical information to be successful, it may not be appropriate to apply the algorithm to data from a single NEXRAD WSR-88D because of both a lack of vertical coverage and resolution degradation at larger distances from the radar. However, the SL3D algorithm can be applied to any gridded volumetric radar dataset so long as the vertical resolution of the dataset is sufficient ($\leq$1-km grid spacing) and the depth

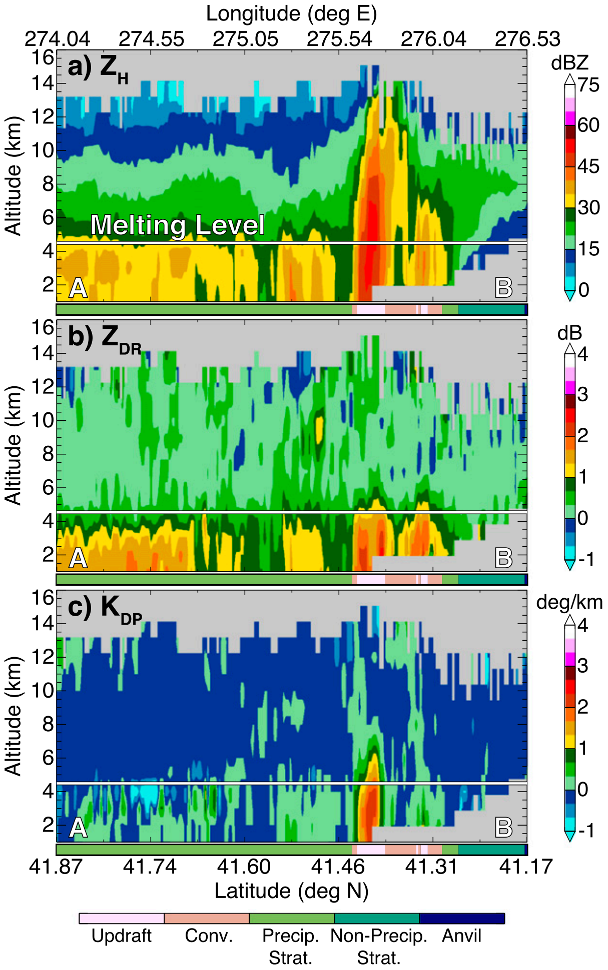

FIG. 11. Vertical cross sections of (a) Z_H, (b) Z_{DR}, and (c) K_{DP} along the line in Fig. 10, from A (left) to B (right). The thick horizontal line in each cross section represents the altitude of the environmental melting level and the thick colored line at the base of each cross section shows the corresponding SL3D classification.

of the volume spans altitudes from 3 to 10 km (as required by the classification categories). In addition, one potential issue for application of the SL3D algorithm related to grid resolution is the sensitivity of the convective classification to the melting-level altitude. Namely, for datasets with vertical resolution that meets or exceeds the uncertainty in the altitude of the melting level used, the $Z_H = 45$ dBZ above the melting level criterion may be erroneously met when the melting-level altitude is underestimated. However, it is worth noting here that this criterion was rarely responsible for convective classifications beyond those identified by the peakedness and echo-top criteria for the cases shown in this study. Thus, while this is a possible limitation of the algorithm, we expect that in most cases it will be negligible.

8. Summary and discussion

This study introduced a new storm classification algorithm for single- and dual-polarization radar observations that leverages three-dimensional information of a volumetric dataset: the SL3D algorithm. Several cases of varying intensity, complexity, and regionality were presented to demonstrate the performance of the algorithm. Comparisons between the SL3D algorithm and a traditional storm classification method (Steiner et al. 1995) revealed that convective regions were commonly larger in scale when using the SL3D classification. This difference was shown to commonly be the result of including echo-top information in the classification and is dependent on the degree of vertical tilt of convection. For cases of less intense convection that traditional methods were unable to detect, the SL3D algorithm was successful in their identification (e.g., see Figs. 7–9). Both the increased frequency of identifying convection and the larger convective regions may have an important impact on the latent heating budget of convective systems (e.g., Houze 1989), especially for latent heat retrievals utilizing two-dimensional methods to aid in the discrimination of echo (e.g., Tao et al. 1993, 2001).

In addition, we introduced a novel three-part convective updraft identification method that leverages both single- and dual-polarization radar information and enables identification of updrafts within storms of varying intensity and complexity. For single-polarization radar, we employed a WER identification method, which was shown to perform well in supercell storms but was unable to routinely identify updrafts in cases with alternative convective organization. For dual-polarization radar observations, the addition of Z_{DR} and K_{DP} column detection was shown to enable updraft identification within most cases of classified convection extending above the melting level (see Figs. 1, 2, 8, 9, 10, and 11). The updraft identification method may be useful for studies investigating the variability of convection and validation of simulated convection in numerical models (e.g., Collis et al. 2013; Varble et al. 2014).

Since SL3D enables the classification of radar echo into five dynamically and physically based categories, it allows for targeted research on individual elements of a storm. For example, previous convective transport studies have found that Z_H of ice within anvil regions can be used as a proxy for identifying the level of maximum detrainment (e.g., Mullendore et al. 2009; Carletta et al. 2016). Because of the inclusion of an ice-only anvil classification, the SL3D algorithm may enable future improvements in this research. Finally, since the SL3D classification leverages three-dimensional radar observations to classify storms, this approach can be applied globally using satellite-based radar observations from systems such as the Tropical Rainfall Measuring Mission (TRMM) Precipitation Radar (PR) or the Global Precipitation Measurement (GPM) mission Dual-Frequency Precipitation Radar (DPR) for a variety of scientific studies.

Acknowledgments. We thank two anonymous reviewers and M. Kumjian at The Pennsylvania State University for providing constructive comments on the manuscript. We would also like to thank Brett Basarab from Colorado State University for providing the DC3 dual-Doppler data. MS and GLM were supported by the National Science Foundation (NSF) under Grant AGS-1432930. CRH was supported by the NSF under Grant AGS-1522910.

REFERENCES

Adler, R. F., and A. J. Negri, 1988: A satellite infrared technique to estimate tropical convective and stratiform rainfall. *J. Appl. Meteor.*, **27**, 30–51, doi:10.1175/1520-0450(1988)027<0030:ASITTE>2.0.CO;2.

Alexander, M. J., 2004: Gravity waves generated by convection in the Darwin area during the Darwin Area Wave Experiment. *J. Geophys. Res.*, **109**, D20S04, doi:10.1029/2004JD004729.

Anagnostou, E. N., 2004: A convective/stratiform precipitation classification algorithm for volume scanning weather radar observations. *Meteor. Appl.*, **11**, 291–300, doi:10.1017/S1350482704001409.

——, and C. Kummerow, 1997: Stratiform and convective classification of rainfall using SSM/I 85-GHz brightness temperature observations. *J. Atmos. Oceanic Technol.*, **14**, 570–575, doi:10.1175/1520-0426(1997)014<0570:SACCOR>2.0.CO;2.

Balakrishnan, N., and D. S. Zrnić, 1990: Estimates of rain and hail rates in mixed-phase precipitation. *J. Atmos. Sci.*, **47**, 565–583, doi:10.1175/1520-0469(1990)047<0565:EORAHR>2.0.CO;2.

Barth, M. C., S.-W. Kim, W. C. Skamarock, A. L. Stuart, K. E. Pickering, and L. E. Ott, 2007: Simulations of the redistribution of formaldehyde, formic acid, and peroxides in the 10 July 1996 Stratospheric-Tropospheric Experiment: Radiation, aerosols, and ozone deep convection storm. *J. Geophys. Res.*, **112**, D13310, doi:10.1029/2006JD008046.

——, and Coauthors, 2015: The Deep Convective Clouds and Chemistry (DC3) field campaign. *Bull. Amer. Meteor. Soc.*, **96**, 1281–1309, doi:10.1175/BAMS-D-13-00290.1.

Basarab, B. M., 2015: Prediction of total lightning in Colorado and Alabama thunderstorms based on storm dynamical and microphysical variables. M.S. thesis, Dept. of Atmospheric Science, Colorado State University, 109 pp. [Available online at https://dspace.library.colostate.edu/handle/10217/166859.]

——, S. A. Rutledge, and B. R. Fuchs, 2015: An improved lightning flash rate parameterization developed from Colorado DC3 thunderstorm data for use in cloud-resolving chemical transport models. *J. Geophys. Res. Atmos.*, **120**, 9481–9499, doi:10.1002/2015JD023470.

Biggerstaff, M. I., and S. A. Listemaa, 2000: An improved scheme for convective/stratiform echo classification using radar reflectivity. *J. Appl. Meteor.*, **39**, 2129–2150, doi:10.1175/1520-0450(2001)040<2129:AISFCS>2.0.CO;2.

Brandes, E. A., J. Vivekanandan, J. D. Tuttle, and C. J. Kessinger, 1995: A study of thunderstorm microphysics with multiparameter radar and aircraft observations. *Mon. Wea. Rev.*, **123**, 3129–3143, doi:10.1175/1520-0493(1995)123<3129:ASOTMW>2.0.CO;2.

Braun, S. A., and R. A. Houze Jr., 1994: The transition zone and secondary maximum of radar reflectivity behind a midlatitude squall line: Results retrieved from Doppler radar data. *J. Atmos. Sci.*, **51**, 2733–2755, doi:10.1175/1520-0469(1994)051<2733:TTZASM>2.0.CO;2.

Bringi, V. N., and V. Chandrasekar, 2001: *Polarimetric Doppler Weather Radar.* 1st ed. Cambridge University Press, 636 pp.

——, D. A. Burrows, and S. M. Menon, 1991: Multiparameter radar and aircraft study of raindrop spectral evolution in warm-based clouds. *J. Appl. Meteor.*, **30**, 853–880, doi:10.1175/1520-0450(1991)030<0853:MRAASO>2.0.CO;2.

——, C. R. Williams, M. Thurai, and P. T. May, 2009: Using dual-polarized radar and dual-frequency profiler for DSD characterization: A case study from Darwin, Australia. *J. Atmos. Oceanic Technol.*, **26**, 2107–2122, doi:10.1175/2009JTECHA1258.1.

Browning, K. A., and R. J. Donaldson, 1963: Airflow and structure of a tornadic storm. *J. Atmos. Sci.*, **20**, 533–545, doi:10.1175/1520-0469(1963)020<0533:AASOAT>2.0.CO;2.

Calhoun, K. M., D. R. MacGorman, C. L. Ziegler, and M. I. Biggerstaff, 2013: Evolution of lightning activity and storm charge relative to dual-Doppler analysis of a high-precipitation supercell storm. *Mon. Wea. Rev.*, **141**, 2199–2223, doi:10.1175/MWR-D-12-00258.1.

Carletta, N. D., G. L. Mullendore, M. Starzec, B. Xi, Z. Feng, and X. Dong, 2016: Determining the best method for estimating the observed level of maximum detrainment based on radar reflectivity. *Mon. Wea. Rev.*, **144**, 2915–2926, doi:10.1175/MWR-D-15-0427.1.

Caylor, I. J., and A. J. Illingworth, 1987: Radar observations and modeling of warm rain initiation. *Quart. J. Roy. Meteor. Soc.*, **113**, 1171–1191, doi:10.1002/qj.49711347806.

Churchill, D. D., and R. A. Houze Jr., 1984: Development and structure of winter monsoon cloud clusters on 10 December 1978. *J. Atmos. Sci.*, **41**, 933–960, doi:10.1175/1520-0469(1984)041<0933:DASOWM>2.0.CO;2.

Collis, S., A. Protat, P. T. May, and C. Williams, 2013: Statistics of storm updraft velocities from TWP-ICE including verification with profiling measurements. *J. Appl. Meteor. Climatol.*, **52**, 1909–1922, doi:10.1175/JAMC-D-12-0230.1.

Conway, J. W., and D. S. Zrnić, 1993: A study of embryo production and hail growth using dual-Doppler and multiparameter radars. *Mon. Wea. Rev.*, **121**, 2511–2528, doi:10.1175/1520-0493(1993)121<2511:ASOEPA>2.0.CO;2.

Crum, T. D., and R. L. Alberty, 1993: The WSR-88D and the WSR-88D Operational Support Facility. *Bull. Amer. Meteor. Soc.*, **74**, 1669–1687, doi:10.1175/1520-0477(1993)074<1669:TWATWO>2.0.CO;2.

Cunningham, J. G., W. D. Zittel, R. R. Lee, and R. L. Ice, 2013: Methods for identifying systematic differential reflectivity (Z_{DR}) biases on the operational WSR-88D network. *36th Conf. on Radar Meteorology*, Breckenridge, CO, Amer. Meteor. Soc., 9B.5. [Available online at https://ams.confex.com/ams/36Radar/webprogram/Paper228792.html.]

DeMott, C. A., and S. A. Rutledge, 1998: The vertical structure of TOGA COARE convection. Part I: Radar echo distribution. *J. Atmos. Sci.*, **55**, 2730–2747, doi:10.1175/1520-0469(1998)055<2730:TVSOTC>2.0.CO;2.

——, R. Cifelli, and S. A. Rutledge, 1995: An improved method for partitioning radar data into convective and stratiform components. Preprints, *27th Conf. on Radar Meteorology*, Vail, CO, Amer. Meteor. Soc., 236–266.

Doviak, R. J., and D. S. Zrnić, 1993: *Doppler Radar and Weather Observations.* 2nd ed. Dover, 562 pp.

Feng, Z., X. Dong, B. Xi, C. Schumacher, P. Minnis, and M. Khaiyer, 2011: Top-of-atmosphere radiation budget of convective core/stratiform rain and anvil clouds from deep convective systems. *J. Geophys. Res.*, **116**, D23202, doi:10.1029/2011JD016451.

Frederick, K., and C. Schumacher, 2008: Anvil characteristics as seen by C-POL during the Tropical Warm Pool International Cloud Experiment (TWP-ICE). *Mon. Wea. Rev.*, **136**, 206–222, doi:10.1175/2007MWR2068.1.

Giangrande, S. E., J. M. Krause, and A. V. Ryzhkov, 2008: Automatic designation of the melting layer with a polarimetric prototype of the WSR-88D radar. *J. Appl. Meteor.*, **47**, 1354–1364, doi:10.1175/2007JAMC1634.1.

Herzegh, P. H., and A. R. Jameson, 1992: Observing precipitation through dual-polarization radar measurements. *Bull. Amer. Meteor. Soc.*, **73**, 1365–1374, doi:10.1175/1520-0477(1992)073<1365:OPTDPR>2.0.CO;2.

Homeyer, C. R., 2014: Formation of the enhanced-V infrared cloud-top feature from high-resolution three-dimensional radar observations. *J. Atmos. Sci.*, **71**, 332–348, doi:10.1175/JAS-D-13-079.1.

——, and M. R. Kumjian, 2015: Microphysical characteristics of overshooting convection from polarimetric radar observations. *J. Atmos. Sci.*, **72**, 870–891, doi:10.1175/JAS-D-13-0388.1.

——, and Coauthors, 2014: Convective transport of water vapor into the lower stratosphere observed during double-tropopause events. *J. Geophys. Res. Atmos.*, **119**, 10 941–10 958, doi:10.1002/2014JD021485.

Hong, Y., C. D. Kummerow, and W. S. Olson, 1999: Separation of convective and stratiform precipitation using microwave brightness temperature. *J. Appl. Meteor.*, **38**, 1195–1213, doi:10.1175/1520-0450(1999)038<1195:SOCASP>2.0.CO;2.

Houghton, H. G., 1968: On precipitation mechanisms and their artificial modification. *J. Appl. Meteor.*, **7**, 851–859, doi:10.1175/1520-0450(1968)007<0851:OPMATA>2.0.CO;2.

Houze, R. A., Jr., 1989: Observed structure of mesoscale convective systems and implications for large-scale heating. *Quart. J. Roy. Meteor. Soc.*, **115**, 425–461, doi:10.1002/qj.49711548702.

——, 1993: *Cloud Dynamics.* 3rd ed. Academic Press, 573 pp.

——, 1997: Stratiform precipitation in regions of convection: A meteorological paradox? *Bull. Amer. Meteor. Soc.*, **78**, 2179–2196, doi:10.1175/1520-0477(1997)078<2179:SPIROC>2.0.CO;2.

Illingworth, A. J., 1988: The formation of rain in convective clouds. *Nature*, **336**, 754–756, doi:10.1038/336754a0.

Johnson, R. H., 1984: Partitioning tropical heat and moisture budgets into cumulus and mesoscale components: Implications for cumulus parameterization. *Mon. Wea. Rev.*, **112**, 1590–1601, doi:10.1175/1520-0493(1984)112<1590:PTHAMB>2.0.CO;2.

Jorgensen, D. P., M. A. LeMone, and S. B. Trier, 1997: Structure and evolution of the 22 February 1993 TOGA COARE squall line: Aircraft observations of precipitation, circulation, and surface energy fluxes. *J. Atmos. Sci.*, **54**, 1961–1985, doi:10.1175/1520-0469(1997)054<1961:SAEOTF>2.0.CO;2.

Kumjian, M. R., 2013a: Principles and applications of dual-polarization weather radar. Part I: Description of the polarimetric radar variables. *J. Oper. Meteor.*, **1**, 226–242, doi:10.15191/nwajom.2013.0119.

——, 2013b: Principles and applications of dual-polarization weather radar. Part II: Warm and cold season applications. *J. Oper. Meteor.*, **1**, 243–264, doi:10.15191/nwajom.2013.0120.

——, 2013c: Principles and applications of dual-polarization weather radar. Part III: Artifacts. *J. Oper. Meteor.*, **1**, 265–274, doi:10.15191/nwajom.2013.0121.

——, and A. V. Ryzhkov, 2008: Polarimetric signatures in supercell thunderstorms. *J. Appl. Meteor. Climatol.*, **47**, 1940–1961, doi:10.1175/2007JAMC1874.1.

——, A. P. Khain, N. Benmoshe, E. Ilotoviz, A. V. Ryzhkov, and V. T. J. Phillips, 2014: The anatomy and physics of Z_{DR} columns: Investigating a polarimetric radar signature with a spectral bin microphysical model. *J. Appl. Meteor. Climatol.*, **53**, 1820–1843, doi:10.1175/JAMC-D-13-0354.1.

Kuo, Y.-H., and R. A. Anthes, 1984: Mesoscale budgets of heat and moisture in a convective system over the central United States. *Mon. Wea. Rev.*, **112**, 1482–1497, doi:10.1175/1520-0493(1984)112<1482:MBOHAM>2.0.CO;2.

Lang, T. J., and S. A. Rutledge, 2002: Relationships between convective storm kinematics, precipitation, and lightning. *Mon. Wea. Rev.*, **130**, 2492–2506, doi:10.1175/1520-0493(2002)130<2492:RBCSKP>2.0.CO;2.

——, and ——, 2008: Kinematic, microphysical, and electrical aspects of an asymmetric bow-echo mesoscale convective system observed during STEPS 2000. *J. Geophys. Res.*, **113**, D08213, doi:10.1029/2006JD007709.

——, and Coauthors, 2004: Prediction of total lightning in Colorado and Alabama thunderstorms based on storm dynamical and microphysical variables. *Bull. Amer. Meteor. Soc.*, **85**, 1107–1125, doi:10.1175/BAMS-85-8-1107.

Loney, M. L., D. S. Zrnić, J. M. Straka, and A. V. Ryzhkov, 2002: Enhanced polarimetric radar signatures above the melting level in a supercell storm. *J. Appl. Meteor.*, **41**, 1179–1194, doi:10.1175/1520-0450(2002)041<1179:EPRSAT>2.0.CO;2.

Mapes, B., and R. A. Houze Jr., 1993: An integrated view of the 1987 Australian monsoon and its mesoscale convective systems. II: Vertical structure. *Quart. J. Roy. Meteor. Soc.*, **119**, 733–754, doi:10.1002/qj.49711951207.

Markowski, P. M., 2002: Hook echoes and rear-flank downdrafts: A review. *Mon. Wea. Rev.*, **130**, 852–876, doi:10.1175/1520-0493(2002)130<0852:HEARFD>2.0.CO;2.

——, and Y. Richardson, 2010: *Mesoscale Meteorology in Midlatitudes.* Wiley-Blackwell, 424 pp.

Mullendore, G. L., D. R. Durran, and J. R. Holton, 2005: Cross-tropopause tracer transport in midlatitude convection. *J. Geophys. Res.*, **110**, D06113, doi:10.1029/2004JD005059.

——, A. J. Homann, K. Bevers, and C. Schumacher, 2009: Radar reflectivity as a proxy for convective mass transport. *J. Geophys. Res.*, **114**, D16103, doi:10.1029/2008JD011431.

Musil, D. J., A. J. Heymsfield, and P. L. Smith, 1986: Microphysical characteristics of a well-developed weak echo region in a High Plains supercell thunderstorm. *J. Climate Appl. Meteor.*, **25**, 1037–1051, doi:10.1175/1520-0450(1986)025<1037:MCOAWD>2.0.CO;2.

National Weather Service, 1991: NOAA Next Generation Radar (NEXRAD) level II base data. NOAA/National Centers for Environmental Information, accessed May 2015 to January 2016, doi:10.7289/V5W9574V.

Nuret, M., and M. Chong, 1998: Characteristics of heat and moisture budgets of a mesoscale convective system observed during TOGA-COARE. *Quart. J. Roy. Meteor. Soc.*, **124**, 1163–1181, doi:10.1002/qj.49712454807.

O'Brien, J. J., 1970: Alternative solutions to the classical vertical velocity problem. *J. Appl. Meteor.*, **9**, 197–203, doi:10.1175/1520-0450(1970)009<0197:ASTTCV>2.0.CO;2.

Park, H., A. V. Ryzhkov, D. S. Zrnić, and K.-E. Kim, 2009: The hydrometeor classification algorithm for the polarimetric WSR-88D: Description and application to an MCS. *Wea. Forecasting*, **24**, 730–748, doi:10.1175/2008WAF2222205.1.

Powell, S. W., R. A. Houze Jr., and S. R. Brodzik, 2016: Rainfall-type categorization of radar echoes using polar coordinate reflectivity data. *J. Atmos. Oceanic Technol.*, **33**, 523–538, doi:10.1175/JTECH-D-15-0135.1.

Ryzhkov, A. V., V. B. Zhuravlyov, and N. A. Rybakova, 1994: Preliminary results of X-band polarization radar studies of clouds and precipitation. *J. Atmos. Oceanic Technol.*, **11**, 132–139, doi:10.1175/1520-0426(1994)011<0132:PROXBP>2.0.CO;2.

——, S. E. Giangrande, V. M. Melnikov, and T. J. Schuur, 2005a: Calibration issues of dual-polarization radar measurements. *J. Atmos. Oceanic Technol.*, **22**, 1138–1155, doi:10.1175/JTECH1772.1.

——, T. J. Schuur, D. W. Burgess, P. L. Heinselman, S. E. Giangrande, and D. S. Zrnić, 2005b: The Joint Polarization Experiment: Polarimetric rainfall measurements and hydrometeor classification. *Bull. Amer. Meteor. Soc.*, **86**, 809–824, doi:10.1175/BAMS-86-6-809.

Scharfenberg, K. A., and Coauthors, 2005: The Joint Polarization Experiment: Polarimetric radar in forecasting and warning decision making. *Wea. Forecasting*, **20**, 775–788, doi:10.1175/WAF881.1.

Schumacher, C., and R. A. Houze Jr., 2003: Stratiform rain in the tropics as seen by the TRMM Precipitation Radar. *J. Climate*, **16**, 1739–1756, doi:10.1175/1520-0442(2003)016<1739:SRITTA>2.0.CO;2.

——, ——, and I. Kraucunas, 2004: The tropical dynamical response to latent heating estimates derived from the TRMM Precipitation Radar. *J. Atmos. Sci.*, **61**, 1341–1358, doi:10.1175/1520-0469(2004)061<1341:TTDRTL>2.0.CO;2.

——, S. N. Stevenson, and C. R. Williams, 2015: Vertical motions of the tropical convective cloud spectrum over Darwin, Australia. *Quart. J. Roy. Meteor. Soc.*, **141**, 2277–2288, doi:10.1002/qj.2520.

Snyder, J. C., A. V. Ryzhkov, M. R. Kumjian, A. P. Khain, and J. Picca, 2015: A Z_{DR} column detection algorithm to examine convective storm updrafts. *Wea. Forecasting*, **30**, 1819–1844, doi:10.1175/WAF-D-15-0068.1.

Srinivasan, A. M., S. V. B. Rao, and R. Suresh, 2014: Investigation of convectively generated gravity wave characteristics and generation mechanisms during the passage of thunderstorm and squall line over Gadanki (13.5°N, 79.2°E). *Ann. Geophys.*, **32**, 57–68, doi:10.5194/angeo-32-57-2014.

Steiner, M., R. A. Houze Jr., and S. E. Yuter, 1995: Climatological characterization of three-dimensional storm structure from operational radar and rain gauge data. *J. Appl. Meteor.*, **34**, 1978–2007, doi:10.1175/1520-0450(1995)034<1978:CCOTDS>2.0.CO;2.

Straka, J. M., D. S. Zrnić, and A. V. Ryzhkov, 2000: Bulk hydrometeor classification and quantification using polarimetric radar data: Synthesis of relations. *J. Appl. Meteor.*, **39**, 1341–1372, doi:10.1175/1520-0450(2000)039<1341:BHCAQU>2.0.CO;2.

Tao, W.-K., S. Lang, J. Simpson, and R. Adler, 1993: Retrieval algorithms for estimating the vertical profiles of latent heat release: Their applications for TRMM. *J. Meteor. Soc. Japan*, **71**, 685–700.

——, and Coauthors, 2001: Retrieved vertical profiles of latent heat release using TRMM rainfall products for February 1988. *J. Appl. Meteor.*, **40**, 957–982, doi:10.1175/1520-0450(2001)040<0957:RVPOLH>2.0.CO;2.

Van Lier-Walqui, M., and Coauthors, 2016: On polarimetric radar signatures of deep convection for model evaluation: Columns of specific differential phase observed during MC3E. *Mon. Wea. Rev.*, **144**, 737–758, doi:10.1175/MWR-D-15-0100.1.

Varble, A., and Coauthors, 2014: Evaluation of cloud-resolving and limited area model intercomparison simulations using TWP-ICE observations: 1. Deep convective updraft properties. *J. Geophys. Res. Atmos.*, **119**, 13 891–13 918, doi:10.1002/2013JD021371.

Williams, C. R., and W. Ecklund, 1995: Classification of precipitating clouds in the tropics using 915-MHz wind profilers. *J. Atmos. Oceanic Technol.*, **12**, 996–1012, doi:10.1175/1520-0426(1995)012<0996:COPCIT>2.0.CO;2.

Yang, Y., X. Chen, and Y. Qi, 2013: Classification of convective/stratiform echoes in radar reflectivity observations using a fuzzy logic algorithm. *J. Geophys. Res. Atmos.*, **118**, 1896–1905, doi:10.1002/jgrd.50214.

Zrnić, D. S., and A. V. Ryzhkov, 1999: Polarimetry for weather surveillance radars. *Bull. Amer. Meteor. Soc.*, **80**, 389–406, doi:10.1175/1520-0477(1999)080<0389:PFWSR>2.0.CO;2.

——, A. Ryzhkov, J. Straka, Y. Lui, and J. Vivekanandan, 2001: Testing a procedure for automatic classification of hydrometeor types. *J. Atmos. Oceanic Technol.*, **18**, 892–913, doi:10.1175/1520-0426(2001)018<0892:TAPFAC>2.0.CO;2.